The Meteoritical Society

Meteoritics & Planetary Science 43, Nr 6, 1049–1061 (2008)
Abstract available online at http://meteoritics.org

Characterizing and navigating small bodies with imaging data

R. W. GASKELL[1*], O. S. BARNOUIN-JHA[2], D. J. SCHEERES[3], A. S. KONOPLIV[4], T. MUKAI[5], S. ABE[10], J. SAITO[9], M. ISHIGURO[6], T. KUBOTA[6], T. HASHIMOTO[6], J. KAWAGUCHI[6], M. YOSHIKAWA[6], K. SHIRAKAWA[7], T. KOMINATO[7], N. HIRATA[8], and H. DEMURA[8]

[1]Planetary Science Institute, 1700 E. Ft. Lowell Rd., Suite 106, Tucson, Arizona 85712, USA
[2]The Johns Hopkins University, Applied Physics Laboratory, Johns Hopkins Road, Laurel, Maryland 20723–6099, USA
[3]Department of Aerospace Engineering Sciences, Colorado Center for Astrodynamics Research, The University of Colorado, 429 UCB, Boulder, Colorado 80309–0429, USA
[4]M. S. 301–121, Jet Propulsion Laboratory, 4800 Oak Grove Drive, Pasadena, California 91109, USA
[5]Graduate School of Science and Technology, Kobe University, Kobe 657-8501, Japan
[6]Japan Aerospace Exploration Agency, Institute of Space and Astronautical Science, Department of Spacecraft Engineering, 3-1-1 Yoshinodai, Sagamihara, Kanagawa 229-8510, Japan
[7]NEC Aerospace Systems,1–10 Nissincho, Fuchu, Tokyo 183-8551, Japan
[8]School of Computer Science and Engineering Ikki-machi, Aizu-Wakamatsu City, University of Aizu, Fukushima 965-8580, Japan
[9]Research and Development Center, PASCO Corporation, 2-8-10 Higashiyama, Meguro-ku, Tokyo 153-0043, Japan
[10]Graduate Institute of Astronomy, National Central University, No. 300, Jhongda Rd., Jhongli City, Taoyuan County 320, Taiwan
[*]Corresponding author. E-mail: rgaskell@psi.edu

(Received 30 January 2007; revision accepted 31 July 2008)

Abstract–Recent advances in the characterization of small body surfaces with stereophotoclinometry are discussed. The principal data output is an ensemble of landmark maps (L-maps), high-resolution topography/albedo maps of varying resolution that tile the surface of the body. Because they can have a resolution comparable to the best images, and can be located on a global reference frame to high accuracy, L-maps provide a significant improvement in discriminatory power for studies of small bodies, ranging from regolith processes to interior structure. These techniques are now being used to map larger bodies such as the Moon and Mercury.

L-maps are combined to produce a standard global topography model (GTM) with about 1.57 million vectors and having a wide variety of applications. They can also be combined to produce high-resolution topography maps that describe local areas with much greater detail than the GTM. When combined with nominal predictions from other data sources and available data from other instruments such as LIDAR or RADAR, solutions for the spacecraft position and camera pointing are the most accurate available. Examples are drawn from studies of Phobos, Eros, and Itokawa, including surface characterization, gravity analysis, spacecraft navigation, and incorporation of LIDAR or RADAR data. This work has important implications for potential future missions such as Deep Interior and the level of navigation and science that can be achieved.

INTRODUCTION

Missions such as Deep Interior (Asphaug et al. 2003), which would have mapped the interior of a small asteroid with radar tomography, require a detailed knowledge of both shape and surface topography of the body as well as accurate determinations of the spacecraft position. Recent applications of stereophotoclinometry and navigation estimation to small bodies have proven to be more than adequate for satisfying the requirements of such missions. During the recent Hayabusa mission to Itokawa, about 600 AMICA science images were analyzed. The asteroid's shape and topography were determined to a resolution of about 40 cm with uncertainties of about 20 cm, and the spacecraft's position was found to a few meters at the home position range of 7 km. For such small bodies, an additional data type such as laser or radar ranging may be used to set the global scale.

A major input to the navigation filter for a spacecraft in proximity to a small body is a set of landmarks or control points, fixed points on the body's surface that can be identified in several images. If the spacecraft positions and orientations are known for these images, the body-fixed location of such a

point can be found through stereographic analysis. In practice, a nominal location is chosen for the landmark and its image-space positions predicted. The set of residuals, differences between predicted and observed locations in the images, is minimized in the least squares sense to estimate the landmark's actual location. For navigation, knowledge of the body-fixed landmark locations is assumed, and a nominal spacecraft state is chosen for a particular image. Residuals between the predicted and observed image-space landmark locations are minimized to estimate the actual spacecraft state. Of course, neither the landmark locations nor the spacecraft states are known precisely, and the uncertainties in these values are included as the entire system of many landmarks in many images is iterated to achieve a best fit.

There are a number of schemes for choosing landmarks. The NEAR mission used craters in this role (Owen et al. 2001) and more recent studies (Ansar et al. 2005) have attempted to automate this process. However, craters are only useful as landmarks if they exist, and the Hayabusa mission to asteroid Itokawa demonstrated that this is not always the case (Honda et al. 2006). Other techniques (Gwinner et al. 2005) automatically identify features of interest and correlate these between several images for stereographic analysis. This method requires images with similar illumination and resolution and with only moderate stereo separation, leading to large absolute uncertainties. Both of these techniques suffer a significant loss of resolution relative to the imaging data since many pixels are needed to specify a single surface point.

This paper describes a new technique that has been developed over the last two decades (Gaskell 1988, 2001, 2002). A landmark/control point is defined as the center of a small digital topography/albedo map (L-map) determined from multiple images with stereophotoclinometry (SPC). Because of their three-dimensional structure, L-maps can be rendered over a wide range of viewing geometries, illuminations, and ranges, and the resulting artificial image correlated with the corresponding actual imaging data. They therefore act as a bridge for correlating widely diverse images and locating their common control points. Since the L-maps are rigid structures, it is not even necessary for the entire L-map to be contained within an image so that sometimes two images are co-registered even though they contain no common surface points. In addition, L-maps can be precisely located on lit limbs, providing nearly 90° of stereo separation, and can be cross-correlated with topography from other L-maps for additional constraints on the solution. The control point locations are therefore determined to a much higher precision in the body-fixed frame, with a corresponding reduction in spacecraft state uncertainty in the navigation solution. Since they can represent any type of surface, the control points can be found anywhere on the body, with the L-maps describing the surrounding topography and albedo variations to nearly the resolution of the best images. Finally, since L-maps accurately describe the topography of the surface, other data types such as laser or radar ranging can be incorporated into the solution.

Stereophotoclinometry (SPC) is at the heart of the construction of an L-map. The slope and albedo at each map pixel are determined in a linear estimation solution minimizing the summed square brightness residuals at that pixel in at least three to hundreds of images, each with differing illumination and viewing conditions. The slopes are then integrated to produce a height distribution, with sparsely sampled heights from external sources such as stereo, limbs, and other maps constraining the integration. In practice, these constraining heights adjust the scale of the reflectance function, effecting an extrapolation from known low-resolution heights from stereography to higher-resolution topography from SPC. The single-map problem is embedded into the global one by solving for a set of maps that tile the entire body. The mutual connections of the global ensemble of overlapping maps, along with limb observations, constrain the slope-to-height integrations and control point solutions, and lead to very small formal uncertainties in both surface characterization and spacecraft state.

Errors in camera pointing, spacecraft position, control point location, and rotational kinematics result in distortions of the extracted imaging data used to construct the L-maps, so the first landmarks used are the more obvious ones such as conspicuous rocks and craters and the stereo separation is kept small so that image sampling errors are reduced. At this stage there is not much difference between this method and the others, but as the geometry solution improves with iteration, smaller-scale L-maps can be used and the stereo separations can be increased to provide precise geometry and topography solutions.

A final element in the iteration loop is the construction of the global topography model (GTM). Not only is the overall shape it provides vital for initial gravity estimates for small body proximity operations, but it also provides nominal estimates for new L-maps that allow for their almost immediate convergence. Instead of the traditional triangular plate format, we use a quadrilateral cell whose vertices are connected according to a simple labeling scheme. This eliminates the need for the facet table used in the triangular model. It also allows the model to be made progressively denser, halving the spacing between points at each step and yielding significant computational benefits. Finally, a simple algorithm can transform the model into the triangular form for use in software that accommodates that format.

Ultimately, the ensemble of L-maps is the principal data product, representing vastly more data than the GTM. L-maps can be manipulated to provide other data products, to acts as navigation tie points and to enable accurate mosaics of imaging data. It is envisioned that future small body missions will involve a survey phase during which the surface is characterized and thousands of landmarks are determined,

followed by a proximity phase involving touch-and-go or landing for which the landmarks will be crucial for surface relative navigation. The choice of landmark type will be a major driver for the survey part of the mission. Ordinary stereography desires to obtain images with uniform illumination and resolution and also requires relatively small stereo separation, while SPC desires differing illuminations and can deal with much larger variations in resolution and separation. Despite the several orders of magnitude increase in navigation and surface characterization accuracy afforded by SPC, mission planners persist in using Sun-synchronous orbits in deference to traditional stereography.

TOPOGRAPHY ESTIMATION

The basic data product of this work is the landmark map (L-map), a digital terrain and albedo model of a portion of a surface as in Fig. 1. It is specified by a vector **V** from the center of a body fixed coordinate system to the origin of a local surface (map) coordinate system, by the axes of that coordinate system $\mathbf{u}_i$ (i = 1,3), and by heights h(**x**) and albedos a(**x**) at positions $\mathbf{x} = (x_1,x_2)$ relative to that system. The spacecraft position **W** and the camera coordinate system c_i (i = 1,3) are also specified in body-fixed coordinates.

For a simple narrow angle camera with focal length f, the location $\mathbf{X} = (X_1, X_2)$ of the image on the focal plane of a point $\mathbf{P} = (\mathbf{x}, h)$ on the surface is given by

$$X_i = f((\mathbf{V}-\mathbf{W})\bullet\mathbf{c}_i + M_{i1}x_1 + M_{i2}x_2 + M_{i3}h)/ ((\mathbf{V}-\mathbf{W})\bullet\mathbf{c}_3 + M_{31}x_1 + M_{32}x_2 + M_{33}h) \quad (1)$$

where $M_{ij} = \mathbf{c}_i\bullet\mathbf{u}_j$, Image data from **X** is therefore associated at map location **x**. $E_k(\mathbf{x})$ designates this extracted data from image k at map location **x**, and is shown in Fig. 2 for a single L-map in several images. The effects of the ortho-rectification process are particularly evident in the second image, where the edge has been distorted due to the height distribution in the L-map, and in the fourth, where portions of crater bottoms are invisible in the image so that data has been set to zero and ignored. Shadows, as in the first two images of Fig. 2, are also ignored.

If the landmarks are already aligned closely enough, to within a few percent of the size of the map, then the map-projected brightness I_k of the kth image can be fit to a simple function of slope, albedo and phase

$$\mathbf{I}_k(\mathbf{x}) = \Lambda_k\mathbf{a}(\mathbf{x})\mathbf{R}(\cos i, \cos e, \alpha) + \Phi_k \quad (2)$$

Since the imaging data is maximally scaled during its extraction, the multiplier Λ_k is included. Moreover, due to background or haze in some images, a positive background term Φ_k can be added. R is an appropriate reflectance function (Hapke 1981; Squyres et al. 1982). The relative albedo a(**x**) is normalized so that <a> = 1 over the map, while *i* and *e* are the

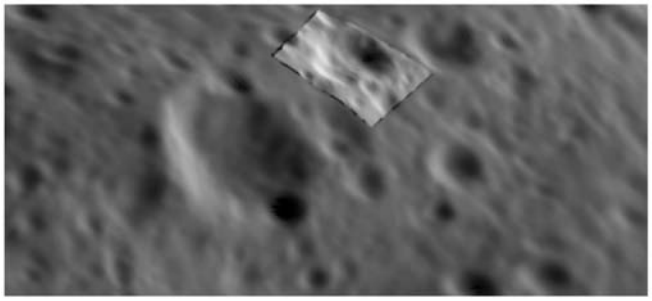

Fig. 1. An L-map on Eros.

angles of incidence and emission relative to the surface normal at **x**. In terms of the slopes $\nabla h = \mathbf{t} = (t_1, t_2)$,

$$\cos i = (s_3 - s_1t_1 - s_2t_2)/\sqrt{\left(1 + t_1^2 + t_2^2\right)},$$
$$\cos e = (e_3 - e_1t_1 - e_2t_2)/\sqrt{\left(1 + t_1^2 + t_2^2\right)} \quad (3)$$

where **s** and **e** are the map-system components of the Sun and spacecraft unit vectors, respectively. A simple mixture of Lambert and Lommel-Seeliger reflectance functions,

$$R(\cos i, \cos e, \alpha) = (1-L(\alpha))\cos i + L(\alpha)\cos i/(\cos i + \cos e) \quad (4)$$

where $L(\alpha) = e^{-\alpha/60}$ is used, with α is in degrees, since it represents well McEwen's (1996) lunar function (Fig. 3). No other phase dependence has been included because only relative brightness is used, and the phase is nearly constant for each L-map in an image. For high albedo surfaces, multiple scattering effects must be included.

At each L-map pixel **x**, the values of **t** and a are estimated by minimizing the weighted sum square residual $\Sigma(E_k(\mathbf{x}) - I_k(\mathbf{x}))^2/\sigma^2$ between the extracted and predicted brightness, where the measurement uncertainty σ is determined from the brightness in the original image, as well as the Λ and Φ. Notice that the slopes determined in this way do not implicitly satisfy the "curl-free" condition $\partial_1 t_2 - \partial_2 t_1 = 0$, which follows from $\partial_1\partial_2 h - \partial_2\partial_1 h = 0$. However, the nominal values of t_1 and t_2 used in the estimation are found from the height solutions described below and are manifestly curl-free, so as the iteration proceeds, the condition is eventually satisfied.

The height h(**x**) is determined from the nearest neighbor heights at $\mathbf{x} + \delta\mathbf{x}_k$ (k = 1, 4) and a possible constraining height h_c coming from the shape model, differential stereography, limb or overlapping map data according to:

$$h(\mathbf{x}) = \left[\sum_{k=1,4}(h(\mathbf{x}+\delta\mathbf{x}_k) - \delta\mathbf{x}_k\bullet(\mathbf{t}(\mathbf{x}) + \mathbf{t}(\mathbf{x}+\delta\mathbf{x}_k))/2) + w_c h_c(\mathbf{x})\right]/(w_c + 4) \quad (5)$$

where w_c is a small constraining weight. This equation is

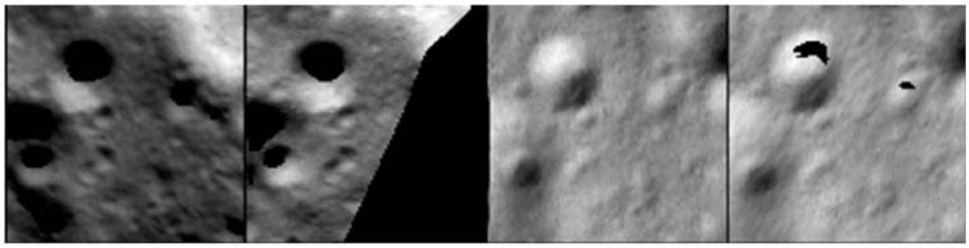

Fig. 2. Extracted data from several images of a landmark map.

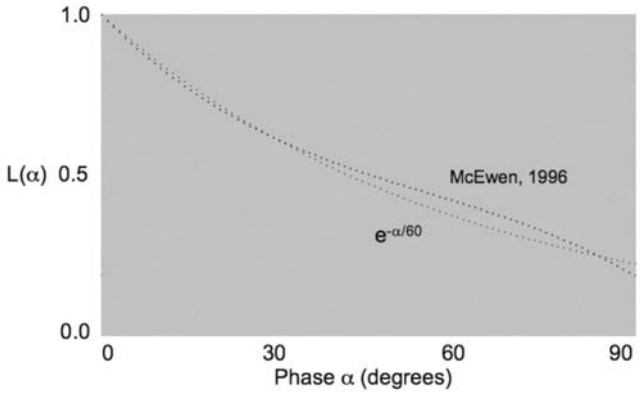

Fig. 3. Simple fit to McEwen's lunar L-function.

applied repeatedly to map points chosen at random until a converged solution is reached. The resulting L-map, viewed with the same geometries and illuminations as the extracted images of Fig. 2, are displayed in Fig. 4.

GEOMETRY ESTIMATION

If the ensemble of landmark vectors **V** were known, as well as their locations **Y** in the image focal plane, then the camera orientation **c** and spacecraft location **W** could be determined. Equation 1 predicts the image space location of an L-map origin as $X_i = f(\mathbf{V} - \mathbf{W}) \bullet \mathbf{c}_i/(\mathbf{V} - \mathbf{W}) \bullet \mathbf{c}_3$ where **W** and **c** are the nominal values. The corrected values $\mathbf{W} + \delta\mathbf{W}$, $\mathbf{c}_i + \varepsilon_{ijk}\mathbf{c}_j\delta\alpha_k$ are determined by minimizing the weighted sum square residuals $\Sigma(\mathbf{Y} - \mathbf{X})^{\mathbf{T}} \bullet \mathbf{M} \bullet (\mathbf{Y} - \mathbf{X})$ between the observed and predicted values, where the sum is over all landmarks in the image. The weighting matrix **M** is determined from the measurement uncertainties in **Y** and the formal uncertainties in the landmark vectors **V**. The observed focal plane locations **Y** are determined by correlating predicted brightness distributions as in Fig. 3 with extracted ones as in Fig. 2.

L-maps whose topographies lie on the lit limb in the image can be used as well. A limb point on the L-map occurs where the line of sight is tangent to the topography, and since its location relative to the origin of the L-map is known, the focal plane location **Y** of the map center can be inferred. At present, no attempt is made to fit the details of the limb, and **M** is chosen to project only the residuals normal to the limb. Since the nominal values for **W** and **c** come from external sources such as a star-tracker, optical navigation and dynamics, additional terms are included in the estimation reflecting these a priori estimates and their uncertainties. Finally, since the spacecraft follows a dynamically determined trajectory, a change in **W** will be accompanied by changes in the positions at neighboring image times. A term reflecting this constraint is also included in the estimation. These contributions are summarized in Equation 6 where S, the quantity to be minimized, is given by the standard estimation (first term), the nominal s/c position and orientation (terms 2 and 3) and the dynamical term.

$$\begin{aligned} S = {} & \Sigma(\mathbf{Y} - \mathbf{X} - \delta\mathbf{W} \bullet \nabla_W\mathbf{X} - \delta\alpha \bullet \nabla_\alpha\mathbf{X})^{\mathbf{T}} \\ & \bullet \mathbf{M} \bullet (\mathbf{Y} - \mathbf{X} - \delta\mathbf{W} \bullet \nabla_W\mathbf{X} - \delta\alpha \bullet \nabla_\alpha\mathbf{X}) + K_n \\ & (\mathbf{W}_n - \mathbf{W} - \delta\mathbf{W})^2 + K_n(\varepsilon_{ijk}\mathbf{c}_{ni} \bullet \mathbf{c}_j - \delta\alpha_k)^2 \\ & + \Sigma K_p(\mathbf{W}_p + \Delta_p - \mathbf{W} - \delta\mathbf{W})^2 \end{aligned} \quad (6)$$

Similarly, if the spacecraft state were known for the ensemble of images, as well as the locations **Y** of a landmark in those images, then the body-fixed vector **V** to that landmark could be determined by solving a set of three coupled linear equations arising from the minimization of the sum square residuals $\Sigma(\mathbf{Y} - \mathbf{X})^{\mathbf{T}} \bullet \mathbf{M} \bullet (\mathbf{Y} - \mathbf{X})$. The sum is now over all images containing the landmark, with **W** and **c** held fixed. As before, the normal limb residuals are included in the solution. The landmark map will generally overlap other maps with central vectors $\mathbf{V}_0$. A correlation with these maps in the overlap region allows the vector $\mathbf{V} - \mathbf{V}_0$ to be determined. This "measurement" is also included in the estimation, and as is evident in Equation 7, it plays a role analogous to the dynamical term in the s/c state estimation.

$$\begin{aligned} S = {} & \Sigma(\mathbf{Y} - \mathbf{X} - \delta\mathbf{V} \bullet \nabla_V\mathbf{X})^{\mathbf{T}} \bullet \mathbf{M} \bullet \\ & (\mathbf{Y} - \mathbf{X} - \delta\mathbf{V} \bullet \nabla_V\mathbf{X}) + \Sigma K_m(\mathbf{V}_m + \Delta_m - \mathbf{V} - \delta\mathbf{V})^2 \end{aligned} \quad (7)$$

The formal uncertainties in camera geometry coming from the solution above feed into the determination of **V**, just as the uncertainties in **V** feed into the determination of **c** and **W**. The assignment of relative weights for image projections, limb projections and map overlaps involves some qualitative assessment of the reliability of the data types. Of course,

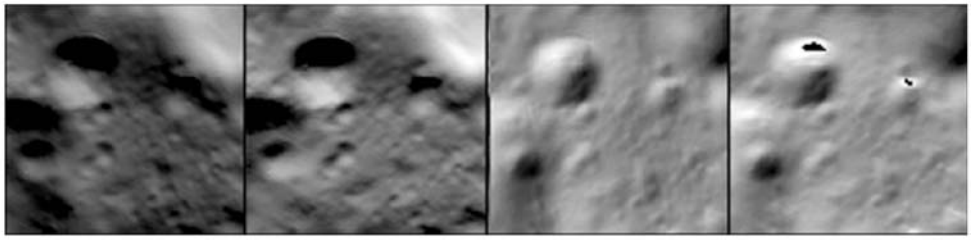

Fig. 4. Illuminated L-map solution.

neither the spacecraft state nor the control point locations are precisely known and the solution process is an iterative one.

A change in the rotation of the body alters the components of the vectors in the body-fixed frame in a time-dependent fashion. It does not affect the scalars $\mathbf{W} \bullet \mathbf{c}$ in Equation 1 since both vectors are associated with a single image and are transformed in the same way. The products $\mathbf{V} \bullet \mathbf{c}$ will change, however, both because the components of $\mathbf{V}$ and $\mathbf{c}$ change and because the new geometry yields a new solution for the L-map vectors. The corrections to the rotational parameters $\mathbf{g}$ and the L-map vectors $\mathbf{V}$ are determined by minimizing

$$S = \Sigma(\mathbf{Y} - \mathbf{X} - \delta\mathbf{g} \bullet \nabla_g\mathbf{X} - \delta\mathbf{V} \bullet \nabla_V\mathbf{X})^{\mathbf{T}} \bullet \mathbf{M} \bullet (\mathbf{Y} - \mathbf{X} - \delta\mathbf{g} \bullet \nabla_g\mathbf{X} - \delta\mathbf{V} \bullet \nabla_V\mathbf{X}) \quad (8)$$

summed over all images and all landmarks. In order to minimize S in Equations 6–8, we take the derivatives with respect to the variations and set them to zero. Equation 8 is of particular interest and the resulting equations are

$$\mathbf{A} \bullet \delta\mathbf{g} + \Sigma\mathbf{C}_k^{\mathbf{T}} \bullet \delta\mathbf{V}_k = \mathbf{r}_0$$

and

$$\mathbf{C}_k \bullet \delta\mathbf{g} + \mathbf{B}_k \bullet \delta\mathbf{V}_k = \mathbf{r}_k \quad (9)$$

where the first two of

$$A = \Sigma(\nabla_g\mathbf{X})^{\mathbf{T}} \bullet \mathbf{M} \bullet (\nabla_g\mathbf{X})\mathbf{r}_0 = \Sigma(\mathbf{Y} - \mathbf{X})^{\mathbf{T}} \bullet \mathbf{M} \bullet (\nabla_g\mathbf{X}), \mathbf{B}_k = \Sigma(\nabla_{Vk}\mathbf{X})^{\mathbf{T}} \bullet \mathbf{M} \bullet (\nabla_{Vk}\mathbf{X}), \mathbf{C}_k = \Sigma(\nabla_{Vk}\mathbf{X})^{\mathbf{T}} \bullet \mathbf{M} \bullet (\nabla_g\mathbf{X}), \mathbf{r}_k = \Sigma(\mathbf{Y} - \mathbf{X})^{\mathbf{T}} \bullet \mathbf{M} \bullet (\nabla_{Vk}\mathbf{X}) \quad (10)$$

are summed over all images and landmarks, and the last three are summed over all images with the landmark fixed at k. In practice, the dV are eliminated from Equation 9 to give

$$(\mathbf{A} - \Sigma\mathbf{C}_k^{\mathbf{T}}\mathbf{B}_k^{-1}\mathbf{C}_k) \bullet \delta\mathbf{g} = \mathbf{r}_0 - \Sigma\mathbf{C}_k^{\mathbf{T}}\mathbf{B}_k^{-1}\mathbf{r}_k \quad (11)$$

which is solved for the rotational correction $\delta\mathbf{g}$. The spacecraft positions $\mathbf{W}$ and orientations $\mathbf{c}$ are then expressed in the new body-fixed frame and Equation 7 is minimized to find the new L-map vectors $\mathbf{V}$. The advantage of this approach is that it involves inversion of a matrix equal in dimension to the number of estimated rotational parameters, but not an additional three times the number of landmarks, which could be in the thousands. The minimizations from Equations 6 and 7 require inversions of six and three-dimensional matrices, respectively.

The solutions for spacecraft position and landmark location contain an overall scale bias that must be resolved with external data. For larger bodies such as Eros, the orbital motion observed with Doppler tracking is sufficient to provide this scale. The known velocities translate into position differences Δ_p for neighboring images which constrains the solution of Equation 6. For smaller bodies such as Itokawa, such a solution is still possible if the spacecraft is allowed to fall toward the surface during Doppler tracking. However, the combination of LIDAR and imaging observations proved to be highly accurate. On Hayabusa, the LIDAR provided a range to the body center that was uncertain by about 50 meters, owing to a lack of shape knowledge. At a range of 10 km, this represented a scale uncertainty of 0.5%. The shape model (GTM) determined from the images therefore had the same 0.5% size uncertainty, representing a scale uncertainty of about a meter, and since the surface location of the LIDAR footprint was precisely known, the range uncertainty dropped to the meter level (0.01%) in one iteration. Further iterations would be useless since the LIDAR uncertainty itself is already about a meter and the GTM surface uncertainty of 16 cm is comparable.

The estimated position uncertainty of the NEAR spacecraft is 10 m. With this as the nominal value and a 1 mrad nominal pointing uncertainty, the formal s/c uncertainties of our solution are reduced to about a meter in position and the 0.025 mrad in attitude. We have been begun including the NLR data in the study. Using about 5000 images with NLR ranges less than 50 km, the NLR bore-sight was located at (259.5,133.4) in the raw images, with the CF-CM of about 10 m and an RMS range residual of 15 m, much smaller than the average GTM resolution of 27 m.

THE GLOBAL TOPOGRAPHY MODEL

As the number of landmarks increases, a nearly rigid network of fixed surface points constrains the solutions for $\mathbf{c}$, $\mathbf{W}$, and $\mathbf{V}$. Moreover, since each L-map contains about

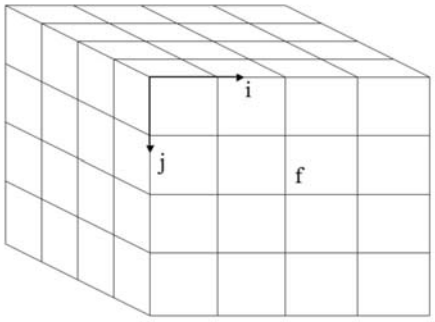

Fig. 5. Implicitly connected quadrilateral (ICQ) labels (q = 4).

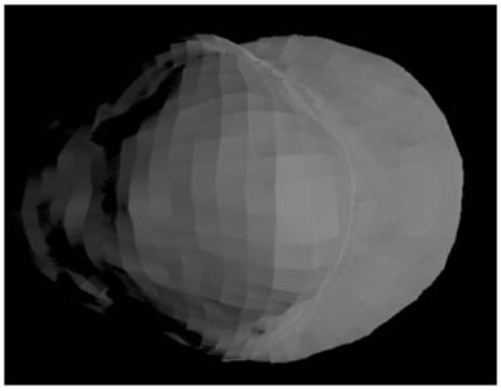

Fig. 6. A reference shape of Eros showing its quadrilateral structure.

10,000 pixels, each at a well-defined location relative to the central vector **V**, the surface is described by a vast amount of data. A common way of organizing this data is as a triangular facet model, which covers the surface with triangular facets whose vertices are vectors lying in the surface. The file representing such a model consists of a numbered list of all vectors in the model, followed by a numbered facet table indicating which vectors form the vertices of each facet.

A useful way of organizing the vectors is in an implicitly connected quadrilateral (ICQ) form. The vectors are labeled and connected to each other as though they were grid points i,j on the faces f of a cube as in Fig. 5, so their labels are i, j, and f where i = 0,q; j = 0,q; f = 1,6. The parameter q is conventionally, but not necessarily, taken to be a power of two, and models are constructed with increasing detail by repeated doubling of q. Models with small values of q, up to 32 or so (about 6000 vectors) are called shape models, while more detailed models are called global topography models (GTMs). There are $6q^2 + 2$ independent vectors in the model, since edges and corners share common vectors, and the vector $\mathbf{v}_{i,j,f}$ is implicitly connected to its nearest neighbors $\mathbf{v}_{i \pm 1,j,f}$ and $\mathbf{v}_{i,j \pm 1,f}$ (if either i or j is on an edge (0 or q), then one of the nearest neighbors will lie on a different face and its label will change accordingly). Not only does this format not require a facet table, making the files about a third as large, its structure also makes it easy to solve some otherwise difficult problems such as determining whether a surface point is illuminated or visible to an observer, and a model is easily interpolated to produce one of the same form with half the point spacing. Moreover, there is a simple program that rewrites the quadrilateral format in the triangular facet format.

The ICQ form is easily displayed in a vertex/facet format with quadrilateral facets. The format begins with a table of $6(q + 1)^2$ numbered vectors with vector $\mathbf{v}_{i,j,k}$ labeled by $L_v(i,j,k) = 1 + i + (q + 1)j + (q + 1)^2 (k–1)$ [(i = 0,q), (j = 0,q), (k = 1,6)]. Appended to this is a facet table numbering the facets and listing the vertices defining them in right-hand-rule order. The $6q^2$ facet labels are $L_f(i,j,k) = i + q(j - 1) + q^2 (k - 1)$ [(i = 1,q), (j = 1,q), (k = 1,6)] and the associated vertex labels are $L_v(i,j,k)$, $L_v(i,j - 1,k)$, $L_v(i - 1,j - 1,k)$, $L_v(i - 1,j,k)$. Some of the vertex labels must be changed in the facet table because they refer to vertices that duplicate others on the edges and corners of the cube. For n = 1,q − 1, 4q − 4 vertex labels are eliminated by replacing

$L_v(0,n,3)$ with $L_v(q,n,4)$ $\quad$ $L_v(q,n,3)$ with $L_v(0,n,2)$
$L_v(0,n,5)$ with $L_v(q,n,2)$ $\quad$ $L_v(q,n,5)$ with $L_v(0,n,4)$

Then, for n = 0,q, 8q + 8 more labels are eliminated by replacing

$L_v(n,0,2)$ with $L_v(n,q,1)$ $\quad$ $L_v(n,0,3)$ with $L_v(0,n,1)$
$L_v(n,0,4)$ with $L_v(q-n,0,1)$ $\quad$ $L_v(n,0,5)$ with $L_v(q,q-n,1)$
$L_v(n,q,2)$ with $L_v(n,0,6)$ $\quad$ $L_v(n,q,3)$ with $L_v(0,q-n,6)$
$L_v(n,q,4)$ with $L_v(q-n,q,6)$ $\quad$ $L_v(n,q,5)$ with $L_v(q,n,6)$

This brings the number of labels down to $6q^2 + 2$. A format with $12q^2$ triangular facets can be constructed by dividing each quadrilateral facet along a diagonal.

The construction of a GTM begins with a low-resolution reference shape such as the one shown in Fig. 6 or, if no previous shape estimate exists, a tri-axial ellipsoid with the approximate dimensions of the body. From each point $\mathbf{v}_p$ of the reference shape, a line is run in the normal direction $\mathbf{n}_p$ until it pierces an L-map at some height h. The normal to the surface at i,j,f is in the direction $(\mathbf{v}_{i,j+1,f} - \mathbf{v}_{i,j-1,f}) \mathbf{x} (\mathbf{v}_{i+1,j,f} - \mathbf{v}_{i-1,j,f})$ (in the special case where i,j,f is a corner (i = 0 or q, j = 0 or q), there are only three nearest neighbors, but the normal is still well defined). The average height $h_p = \langle h \rangle$ of all L-map piercing points defines a new vector

$$\mathbf{V}_p = \mathbf{v}_p + \mathbf{n}_p h_p . \qquad (12)$$

It is important to use this method rather than simply averaging the radius as a function of latitude and longitude because for many small bodies, Eros, and Itokawa in particular, the radii can be multi-valued as a function of direction. In practice, the reference shape is first made denser by halving the spacing of a previous model through bilinear interpolation in each cell.

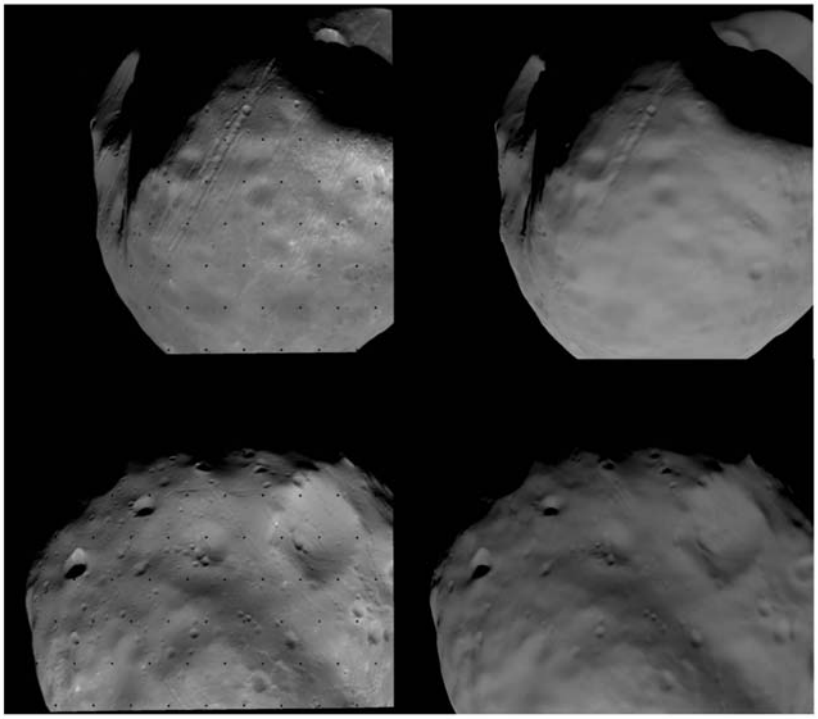

Fig. 7. Viking orbiter images of Phobos (left) and illuminated GTM.

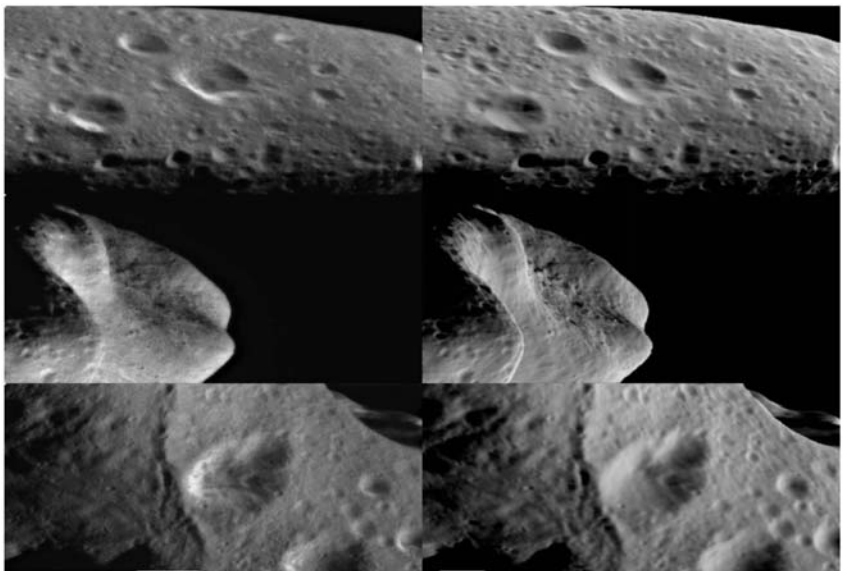

Fig. 8. NEAR images (left) of Eros and illuminated GTM.

The typical initial reference shape has q = 32. This is "densified" to q = 64 and the vectors determined as in Equation 12 to produce a 24578 vector GTM constructed. This becomes a new reference shape and the procedure is repeated to create q = 128, 256 and 512 models, the last having about 1.57 million vectors. Because the first tri-axial reference surfaces were far from the true shape, the distribution of vectors in the final model was not uniform. An algorithm has been developed to more evenly distribute the vectors of subsequent initial shapes. Figures 6 through 9 display images of Phobos, Eros, and Itokawa, respectively, along with corresponding images generated from their GTMs.

APPLICATIONS OF THE GTM

The corner vectors defining a cell on one of the faces of the GTM, $\mathbf{V}_{i,j}$, $\mathbf{V}_{i+1,j}$, $\mathbf{V}_{i,j+1}$ and $\mathbf{V}_{i+1,j+1}$, define an approximate

Table 1. Physical properties of the GTMs.

Body	Volume (km^3)	Area (km^2)	I_{xx}/M (km^2)	I_{yy}/M (km^2)	I_{zz}/M (km^2)
Phobos	5759.91	1650.40	43.79	51.49	60.53
Eros	2507.60	1137.93	15.13	73.09	74.35
Itokawa	0.01773	0.40403	0.00631	0.02128	0.02235

Fig. 9. Hayabusa images (left) of Itokawa and illuminated GTM.

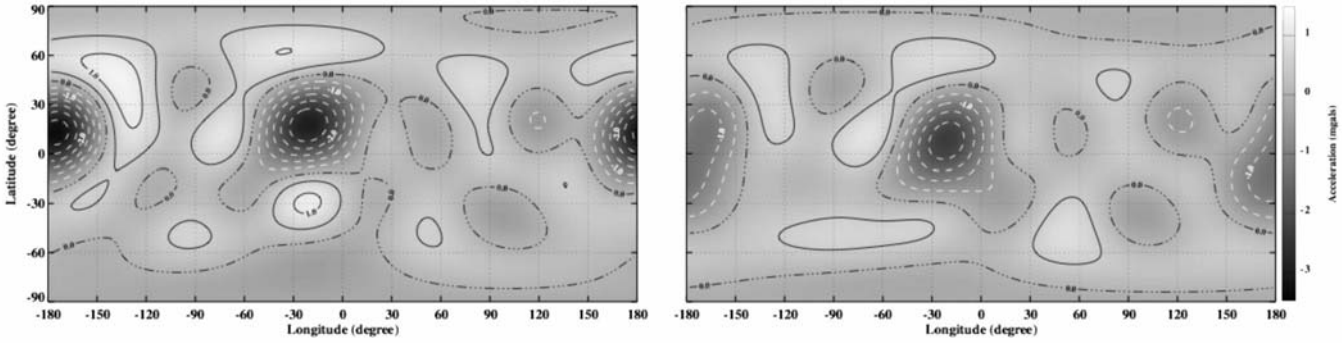

Fig. 10. Eros Bouguer anomalies from NLR shape model (left) and current GTM.

prism. The area vector of the cell is

$$\mathbf{dA} = (\mathbf{V}_{i+1,j+1} - \mathbf{V}_{i,j}) \mathbf{x} (\mathbf{V}_{i+1,j} - \mathbf{V}_{i,j+1})/2. \quad (13)$$

If **V** is the average of the four corner vectors, V is its magnitude, then since $dA << V^2$ for the GTM, the differential solid angle is very nearly

$$d\Omega = \mathbf{V} \bullet d\mathbf{A}/V^3. \quad (14)$$

This allows for very rapid calculations of physical properties of the model such as surface area, volume, moment of inertia tensor, and gravity harmonics. Notice that $d\Omega$ can be negative for some cells, indicating that a radius vector pierces the surface multiple times. The volumes, areas and principal moments for the three GTMs displayed above are summarized in Table 1.

The gravity harmonics for the Eros GTM are easily calculated, assuming a homogeneous mass distribution, and can be compared with those determined from an analysis of the NEAR orbit solution. The Bouguer anomaly, the difference between these two determinations for harmonics L = 2 to L = 6 on a 16 km sphere, are shown in Fig. 10. The NEAR Laser Ranger shape model (Zuber et al. 2000; Miller et al. 2002) produced significant anomalies (Fig. 10, left), which ranged from –3.2 mgal to +1.5 mgal and led to speculations of lower densities near the ends of Eros. The anomalies from our GTM (Fig. 10, right) range from –2.37 mgal to +0.94 mgal, suggesting a much more homogeneous Eros, a result also supported by the small CF-CM offset from the NLR/imaging study discussed earlier.

The gravitational potential at a point **R** not too close to the surface is found by summing the contributions

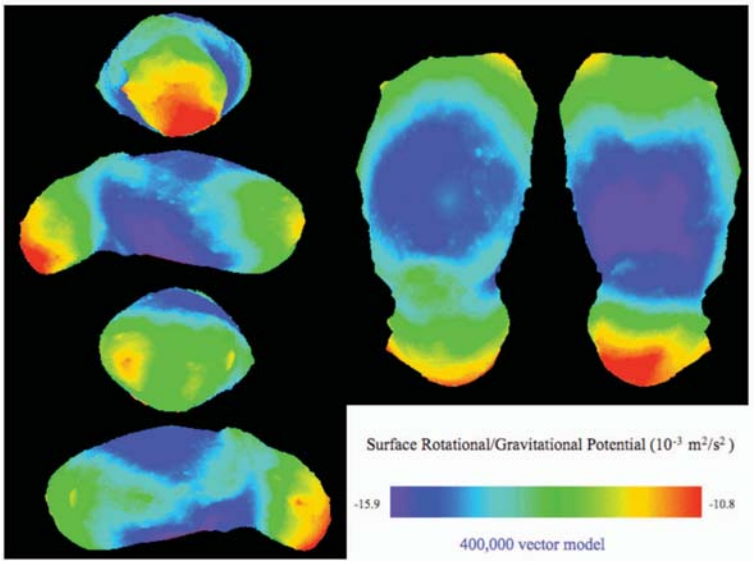

Fig. 11. Rotational/gravitational surface potential distribution for Itokawa.

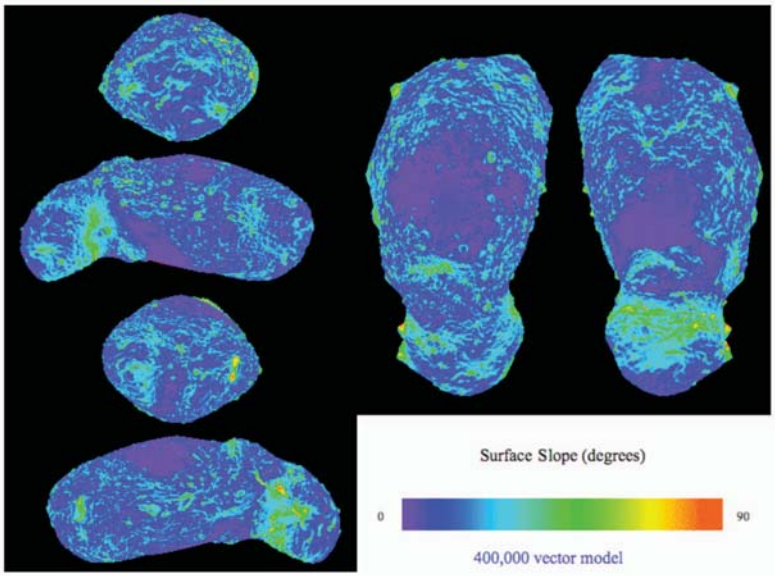

Fig. 12 Surface slope relative to local gravity for Itokawa.

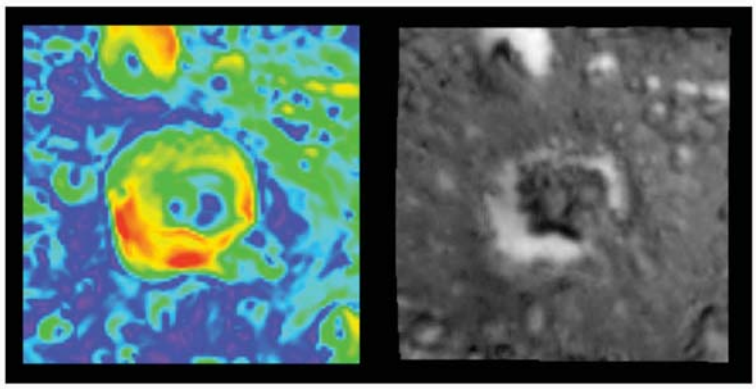

Fig. 13. Local slopes (left) of a topo/albedo L-map (right) on Eros.

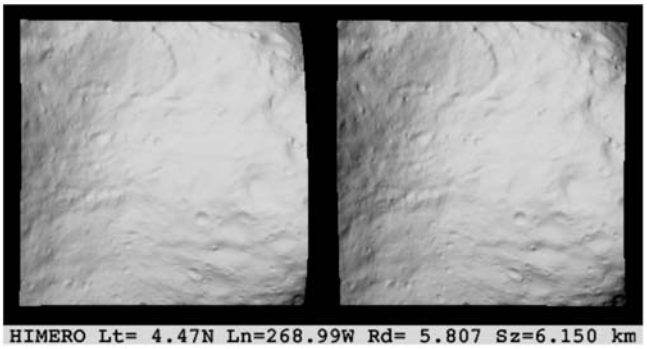

Fig. 14. Stereo pair of HRTM for Himeros Regio on Eros.

$$dU = -(\rho G/2)\mathbf{dA} \bullet (\mathbf{V} - \mathbf{R})/|\mathbf{V} - \mathbf{R}| \quad (15)$$

However, for a point **R** near the surface, one or more of the **dA** will subtend a significant solid angle. The quadrilateral structure of makes it possible to divide a cell into sub-cells by bilinear interpolation, as was done in the "densification" step in the GTM construction. A recursive procedure has been developed that automatically subdivides a cell if, seen from **R**, it subtends an angle larger than a pre-determined limit. An interpolated vector in the cell, with x and y varying from 0 to 1, is

$$V(x, y) = (1 - x)(1 - y)\mathbf{V}_{i,j} + x(1 - y)\mathbf{V}_{i+1,j} + (1 - \mathbf{x})y \mathbf{V}_{i,j+1} + xy\mathbf{V}_{i+1,j+1} = \mathbf{V}_0 + \mathbf{V}_1 x + \mathbf{V}_2 y + \mathbf{V}_3 xy \quad (16)$$

and the area element at x,y is given by

$$d\mathbf{a}(x, y) = (\partial\mathbf{V}/y \times \partial\mathbf{V}/\partial x)dxdy = (\mathbf{A}_0 + \mathbf{A}_1 x + \mathbf{A}_2 y)dxdy \quad (17)$$

The subdivision coefficients $\mathbf{V}_k$ and $\mathbf{A}_k$ are computed and saved for each cell of the GTM, making it possible to rapidly compute the gravitational potential and acceleration at any point **R**. The surface potential, including rotational effects, is shown in Fig. 11 for Itokawa, calculated from the q = 256 (400000 vector) model.

Figure 12 shows the slope distribution relative to the local gravity. Smoother, lower slope areas correspond to lows of the potential, indicating that loose material has migrated to these areas, possibly due to seismic shaking. A similar process operates on Eros, where down-slope motion exposes fresher, brighter material underneath. Figure 13 shows the correlation between gravity-relative slope and albedo for a 5 km square L-map on Eros.

HIGH-RESOLUTION TOPOGRAPHY MAPS

The majority of L-maps on Eros (6850 of 8995) have a resolution of 6 m/pixel. Some L-maps have lower resolution and provide context for the global fit, while others have higher resolution in order to better characterize regions of particular interest. Since the GTM has an average resolution of about 27 m, it does not contain the full information provided by the ensemble of L-maps. High-resolution topography maps (HRTMs) can be constructed from the L-map ensemble for areas of interest, such as the 6-meter resolution 1025 × 1025 pixel topographic map of Himeros Regio shown as a stereo pair in Fig. 14. The construction of an HRTM is similar to that of an L-map or a GTM. At each pixel, the heights and slopes of the contributing L-maps are averaged. A small fraction of the averaged heights is used as constraining heights, and the slopes are integrated as in Equation 5.

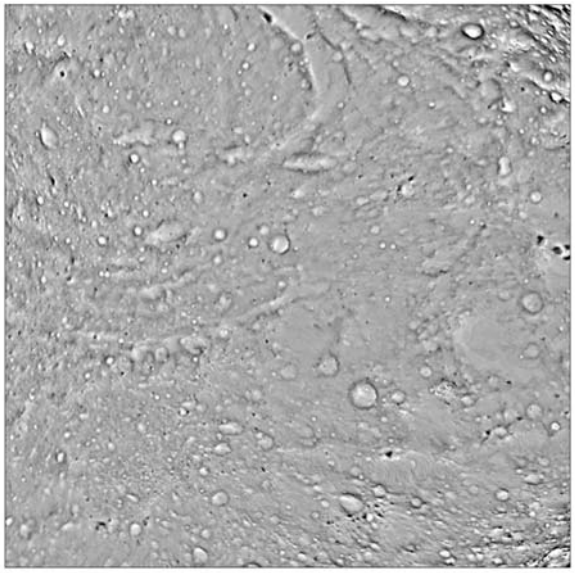

Fig. 15. Laplacian filtered heights $\nabla^2 h$ for Himeros Regio on Eros.

Since HRTMs can be constructed with almost the resolution of the best images, they summarize that data with very little loss of information. These new representations can be recast in a variety of ways to assist in data analysis. The map of Himeros Regio, processed by computing $\nabla^2 h$ from the HRTM data, is shown in Fig. 15. This Laplacian filter is commonly used in analysis of medical X-ray images. It makes craters and boulders are much easier to identify, and this may eventually lead to an automatic cataloging capability. Another way to display data using an HRTM is by re-sampling an image onto its topography. Figures 16 and 17 are stereo pairs of Tsukuba, a cracked rock on Itokawa, and the Pencil boulder, which sticks straight up from the asteroid's surface with a slope of 90° relative to the local gravity.

PROXIMITY NAVIGATION

The ensemble of L-maps was originally conceived as a tool for optical navigation. The iterative minimizations of Equations 6 and 7 determine the spacecraft state and the body-fixed locations of the L-map centers during a survey phase. During the proximity phase, the pre-existing set of L-maps would be correlated with new images, and their resulting focal plane locations used as inputs to determine the

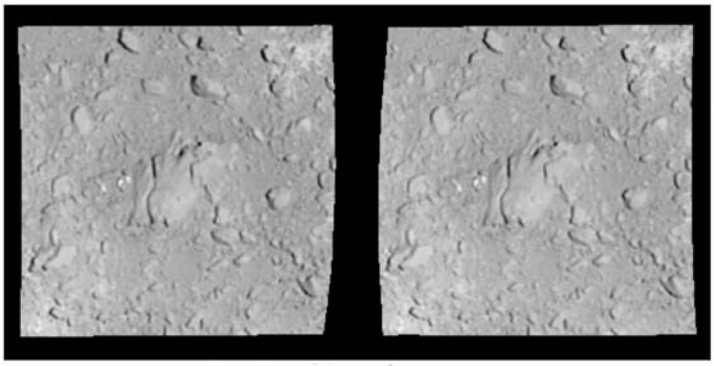

Fig. 16. Stereo pair of Tsukuba rock on Itokawa.

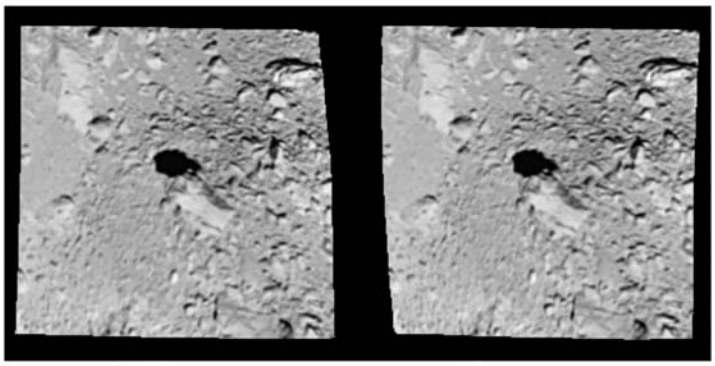

Fig. 17. Stereo pair of the Pencil boulder on Itokawa.

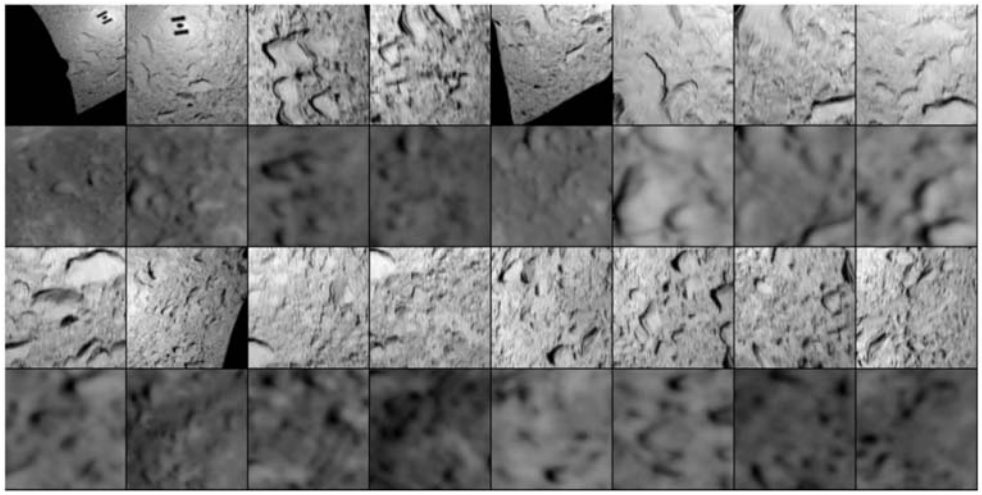

Fig. 18. Extracted image data from a November 12, 2005, wide-angle navigation frame and corresponding Itokawa L-maps.

spacecraft state (Gaskell 2001). This technique was tested with navigation images obtained during the November 12, 2005, approach of Hayabusa to Itokawa. Twelve of the wide-angle Hayabusa navigation frames, with slant ranges varying from 57 m to 740 m, were correlated with L-maps. The RMS difference between the predicted ranges and the measured LIDAR ranges was about 10 m. The final two images in the sequence had the largest errors because the LIDAR was moving off the body. When these two were removed, the RMS residual dropped to 4 m. A display from the L-map correlation of one of these images is shown in Fig. 18, with alternate rows showing extracted imaging data and corresponding L-map data. Note the spacecraft's shadow in the first two boxes. The shadow appeared in ten of the images, and was used to determine the precise camera pointing. Despite the difference in resolution, the very lossy

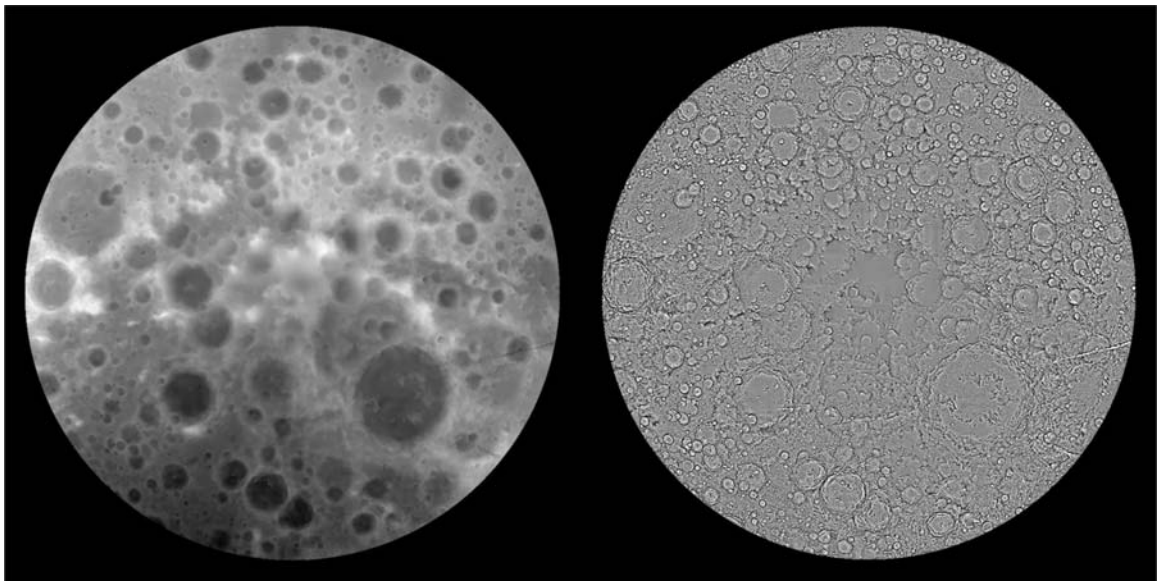

Fig. 19. DEM for lunar south polar region (left) and Laplacian filtered heights (right).

compression of the data, and significant phase changes across the wide-angle frame, the software was able to perform the correlations. A trajectory was fit to the data and used to solve for the mass of Itokawa (Scheeres et al. 2006) with the result $GM = 2.36 \times 10^{-9} \pm 0.15 \times 10^{-9}$ km^3/s^2. With the 0.0177 km^3 volume from the GTM, the density becomes 2.0 g/cm^3, suggesting a porous interior.

It is certainly possible to use RADAR in the place of LIDAR in conjunction with imaging for small body navigation and surface characterization, and to map the interior structure as proposed for Deep Interior. Work in this area is currently being carried out (Safaeinili et al. 2006) and the internal structure of Phobos probed. The model shown in Fig. 7 is being used to remove surface reflections.

BEYOND SMALL BODIES

Work is now under way to investigate the application of these techniques to larger bodies such as the Moon. About 6% of the Moon's surface has been mapped using Clementine data and SPC with over 14,000 L-maps at 500 and 220 m resolution. The RMS position uncertainty of the control points is about 240 m. The Clementine data is a case study in how not to gather data for SPC. Most of the data near the equator was purposely taken at low phase angle, and there was no attempt to gather lower-resolution context images either from higher orbits or oblique pointing. Some Lunar Orbiter images have been used in this region to provide variation in illumination. The situation poleward of 60° N or S is a bit better, with larger stereo separation from oblique viewing and occasionally some useful phase separation. Figure 19 shows the Moon south of about 62.5° S latitude. The left side is a digital elevation map referred to a 1737.4 km sphere, with elevations ranging from −8.40 km to +7.76 km. The right side shows the same data with a Laplacian filter. Smooth areas near the pole and in some deep craters are interpolated because of missing data due to shadowing. When new images becomes available, data covering the existing set of L-maps will be automatically extracted and correlated to produce more precise topography and reduce the position uncertainties.

Image-sequencing strategies for larger bodies differ significantly between traditional stereo and SPC. The former prefers Sun-synchronous orbits with both nadir pointing and along-track off-nadir slews for stereo, in order to have a consistent illumination. The latter requires differing illumination, which can be accomplished in the previous context with cross-track slews, and can handle much larger stereo separation even out to the lit limb. Because of limited stereo separation and a small number of images, traditional stereo is dependent on precise knowledge of the spacecraft state and is capable only of determining relative surface topography at degraded resolution. SPC uses all images at all resolutions, including those with oblique views, and provides absolute topography at full resolution, even in featureless areas where stereo does not work. It also yields improved solutions for the spacecraft state.

Acknowledgments–This research was carried out at the Jet Propulsion Laboratory, California Institute of Technology, under contract with the National Aeronautics and Space Administration, at the Institute of Space and Astronautical Science, Sagamihara, Japan, and at the Planetary Science Institute. We thank Dr. Yasuhiro Yokota at ISAS for his effort on the AMICA operation during the Hayabusa mission phase.

Editorial Handling—Dr. Ellen Beth Clark

REFERENCES

Ansar A. and Cheng Y. 2006. An analysis of spacecraft localization from descent image data for pinpoint landing on Mars and other cratered bodies. *Photogrammetric Engineering and Remote Sensing* 71:1197–1204.

Asphaug E., Belton M. J. S., Cangahuala A., Keith L., Klaasen K., McFadden L., Neumann G., Ostro S. J., Reinert R., Safaeinili A., Scheeres D. J., and Yeomans D. K. 2003. Exploring asteroid interiors: The Deep Interior mission concept (abstract #1906). 34th Lunar and Planetary Science Conference. CD-ROM.

Gaskell R. W. 1988. Digital identification of cartographic control points. *Photogrammetric Engineering and Remote Sensing* 54(6), Part 1:723–727.

Gaskell R. W. 2001. Automated landmark identification for spacecraft navigation. AAS paper 01–422. AAS/AIAA Astrodynamics Specialists Conference, Quebec City, Canada.

Gaskell R. W. 2002. Determination of landmark topography from imaging data. AAS paper 02–021. AAS/AIAA Astrodynamics Specialists Conference, Breckenridge, Colorado.

Gaskell R. W. 2005. Landmark navigation and target characterization in a simulated Itokawa encounter. AAS paper 05–289, AAS/AIAA Astrodynamics Specialists Conference, Lake Tahoe, California, USA.

Gaskell R. W., Saito J., Ishiguro M., Kubota T., Hashimoto T., Hirata N., Abe S., Barnouin-Jha O., and Scheeres D. 2006. Global topography of asteroid 25143 Itokawa (abstract #1876). 37th Lunar and Planetary Science Conference. CD-ROM.

Gaskell R., Barnouin-Jha O., Scheeres D., Mukai T., Hirata N., Abe S., Saito J., Ishiguro M., Kubota T., Hashimoto T., Kawaguchi J., Yoshikawa M., Shirakawa K., and Kominato T. 2006. Landmark navigation studies and target characterization in the Hayabusa encounter with Itokawa. AIAA paper 2006–6660. AAS/AIAA Astrodynamics Specialists Conference, Keystone, Colorado, USA.

Gwinner K., Scholten F., Spiegel M., Schmidt R., Giese B., Oberst J., Jaumann R., and Neukum G. 2005. Derivation of high-resolution topography from Mars Express HRSC data. *Geophysical Research Abstracts* 7:09572.

Hapke B. 1981. Bidirectional reflectance spectroscopy, I. Theory. *Journal of Geophysical Research* 86:3039–3054.

Honda C., Nakamura R., Ishiguro M., Saito J., Hashimoto T., Kubota T., Nakamura A. M., Hirata N., Hiraoka K., Demura H., and Michikami T. 2006. Crater counting on 25143 Itokawa: Preliminary results (abstract #1620). 37th Lunar and Planetary Science Conference. CD-ROM.

McEwen A. J. 1996. A precise lunar photometric function (abstract #1876). 27th Lunar and Planetary Science Conference. pp. 841–842.

Miller J. K., Konopliv A. S., Antreasian P. G., Bordi J. J., Chesley S., Helfrich C. E.,Owen W. M., Wang T. C., Williams B. G., Yeomans D. K., and Scheeres D. J. 2002. Determination of shape, gravity, and rotational state of asteroid 433 Eros. *Icarus* 255:3–17.

Owen W. M. Jr., Wang T. C., Harch A., Bell M., and Peterson C. 2001. NEAR optical navigation at Eros. AAS Paper 01–376. AAS/AIAA Astrodynamics Specialists Conference, Quebec City, Canada.

Safaeinili A., Calaberese D., Cicchetti A., Nenna C., Ivanov A., Gim Y., Duxbury T., Kirchner D., Plettemeier D., Kofman W., Herique A., Heggy E., Hagfors T., Orosei R., Jordan R., Phillips R., Stofan E. R., Gurnett D., Nielsen E., Plaut J. J., and Picardi G. 2006. First radar observation of Phobos by MARSIS. *Geophysical Research Abstracts* 8:05330.

Scheeres D. J., Gaskell R., Abe S., Barnouin-Jha O., Hashimoto T., Kawaguchi J., Kubota T., Saito J.,Yoshikawa M., Hirata N., Mukai T., Ishiguro M., Kominato T., Shirakawa K., and Uo M. 2006. The actual dynamical environment about Itokawa. AIAA paper 2006–6661. AAS/AIAA Astrodynamics Specialists Conference, Keystone, Colorado, USA.

Squyres S. and Veverka J. 1982. Variation of albedo with solar incidence angle on planetary surfaces. *Icarus* 50:115–122.

Zuber M. T., Smith D. E., Cheng A. F., Garvin J. B., Aharonson O., Cole T. D., Dunn P. J., Guo Y., Lemoine F. G., Neumann G. A., Rowlands D. D., and Torrence M. H. 2000. The shape of 433 Eros from the NEAR-Shoemaker Laser Rangefinder. *Science* 289: 2097–2101.